Highly Aligned Epitaxial Nanorods with a Checkerboard Pattern in Oxide Films

S. Park,*[†,‡] Y. Horibe,[†,‡] T. Asada,[†,‡,§] L. S. Wielunski,[‡] N. Lee,[†,‡] P. L. Bonanno,[||]
S. M. O'Malley,[||] A. A. Sirenko,[||] A. Kazimirov,[⊥] M. Tanimura,[§] T. Gustafsson,[‡] and
S.-W. Cheong[†,‡]

*Rutgers Center for Emergent Materials, Rutgers University, Piscataway,
New Jersey 08854, Department of Physics and Astronomy, Rutgers University,
Piscataway, New Jersey 08854, Research Department, NISSAN ARC, LTD.,
Yokosuka, Kanagawa 237-0061, Japan, Department of Physics, New Jersey Institute of
Technology, Newark, New Jersey 07102, and Cornell High Energy Synchrotron Source
(CHESS), Cornell University, Ithaca, New York 14853*

ABSTRACT

One of the central challenges of nanoscience is fabrication of nanoscale structures with well-controlled architectures using planar thin-film technology. Herein, we report that ordered nanocheckerboards in $ZnMnGaO_4$ films were grown epitaxially on single-crystal MgO substrates by utilizing a solid-state method of the phase separation-induced self-assembly. The films consist of two types of chemically distinct and regularly spaced nanorods with mutually coherent interfaces, $\sim 4 \times 4 \times 750$ nm^3 in size and perfectly aligned along the film growth direction. Surprisingly, a significant in-plane strain, more than 2%, from the substrate is *globally* maintained over the entire film thickness of about 820 nm. The strain energy from Jahn–Teller distortions and the film–substrate lattice mismatch induce the coherent three-dimensional (3D) self-assembled nanostructure, relieving the volume strain energy while suppressing the formation of dislocations.

Nanoscale self-organization is used to assemble nanoparticles with precisely controlled size, shape, and composition and is achieved through "wet chemistry" by utilizing organic templates. However, this solution technique has found limited use for fabricating *inorganic* components of technological devices.[1−3] On the other hand, stress-domain dominated self-assembly with nanoscale patterns on solid *surfaces* are intensively studied for potential usage as nanostructure templates.[4−7] In oxide materials, a few approaches have been examined to fabricate self-assembled structures through *solid-state* processes, which may enable new functionalities. For example, films with ferroelectric−ferrimagnetic mixtures, such as $BaTiO_3$−$CoFe_2O_4$,[8] have been successfully grown and have shown remarkable magnetoelectric coupling phenomena.[9] However, the relevant length scale is still larger than 40−60 nm which can be alternatively achieved by current e-beam lithographical techniques, and there exists no structural ordering between compositionally different phases.[10] A new solid-state method of the self-assembly by harnessing Jahn−Teller structural distortions was reported

for polycrystalline spinel $ZnMnGaO_4$ bulk materials.[11] Strain-accommodating interaction between the Mn-rich orthorhombic and Mn-poor cubic regions results in ordered nanorods ($\sim 4 \times 4 \times 70$ nm^3) with a checkerboard pattern (CB). This pure solid-state self-assembly can be ubiquitous in spinels with JT ions, which exhibit a variety of physical phenomena, and thus can be implemented to fabricate heterogeneous nanostructures with new functionalities. In fact, a similar nanocheckerboard structure was also observed in ferrimagnetic $Mg(Mn,Fe)_2O_4$.[12] It is conceivable to utilize the nano-CB consisting of ferrimagnetic spinels with large shape anisotropy for magnetic media for ultrahigh-density perpendicular data storage. In addition, a perovskite oxide showing a two-dimensional CB-like nanostructure has been recently reported, revealing that this nanostructure formation in oxides is not limited to the spinel system.[13] However, the intriguing self-assembly in oxides was observed only in polycrytalline bulk materials: it is evident that the realization of the nanocheckerboard structure in large scale, desirably film forms is a critical step toward technological applications of nano-CB.

We report here the epitaxial growth of thick (~ 820 nm) films of $ZnMnGaO_4$ with well-oriented nano-CB by a simple self-assembly technique. Structurally and chemically distinct Mn-rich and Mn-poor nanorods, perfectly aligned along the

* To whom correspondence should be addressed. Email: floura@physics.rutgers.edu.
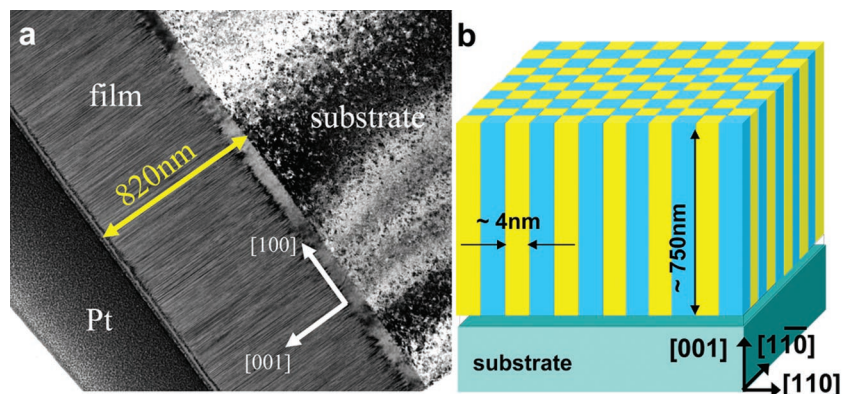† Rutgers Center for Emergent Materials, Rutgers University.
‡ Department of Physics and Astronomy, Rutgers University.
§ NISSAN ARC, LTD.
|| New Jersey Institute of Technology.
⊥ Cornell University.

Figure 1. A self-assembled nanocheckerboard ZnMnGaO$_4$ film grown on a (001) MgO substrate. (a) Transmission electron microscopy (TEM) side-view image of the spinel film at low magnification. The picture is normal to the (010) axis. Pt is used for a capping layer for focused ion beam (FIB) sample preparation. (b) Schematic picture of a well-oriented nanorod spinel film formed on a substrate. The nanorods are aligned along the [001] direction.

film growth direction, stack alternatively to form a periodic CB pattern with mutually coherent interfaces. This unique 3D epitaxy process contrasts with a typical behavior in conventional growth of highly lattice-mismatched films and thus provides an important route for film fabrication of nanostructured arrays with periodically varied electronic and magnetic properties.

ZnMn$_2$O$_4$ forms in a tetragonal structure (space group: $I4_1/amd$, a_c = 8.091 Å, c_c = 9.240 Å), while ZnGa$_2$O$_4$ crystallizes in a cubic structure (space group: $Fd\bar{3}m$, a = 8.330 Å). When they are mixed in ZnMnGaO$_4$ (ZMGO), the high-temperature phase is chemically and structurally homogeneous with a tetragonal distortion (space group: $I4_1/amd$, $a_c \approx 8.2$ Å, $c_c \approx 8.7$ Å). Upon lowering temperature, spinodal phase separation,[14] accompanying Mn^{3+} diffusion within each tetragonal twin domain, results in Mn-rich orthorhombic regions (JT-active ZnMn$_{1.7}$Ga$_{0.3}$O$_4$) and Mn-poor cubic regions (JT-inactive ZnMn$_{0.5}$Ga$_{1.5}$O$_4$). Proper control of the diffusion kinetics changes the balance between the elastic and interfacial energy of the structural variants, and the large misfit between the orthorhombic and cubic phases leads to the nanometer-scale self-assembled CB structure with a high degree of periodicity.[11] Note that annealing time near the JT transition temperature was recently found to be a critical factor in the nanostructure formation of the phase-separated spinels.[15]

ZMGO films were deposited on single crystalline (001) MgO substrates by using a pulsed laser deposition (PLD) technique from a tetragonal ZMGO target. The grown films are ~820 nm thick with an exceptionally smooth surface: the root-mean-square roughness is about 0.7 nm over areas of 3 × 3 μm^2 as determined by atomic force microscopy (AFM). The bright-field transmission electron microscope (TEM) image of the side view of a film in Figure 1a reveals well-ordered fine fringes perpendicular to the substrate surface, demonstrating the formation of vertically oriented nanorods. A schematic picture of stacked nanorods in a ZMGO film on a (001) MgO substrate is illustrated in Figure 1b. The self-assembled square nanorods exhibit a CB pattern in the top view, where the edge of the square is along the [110] crystallographic direction. Yellow and blue colors
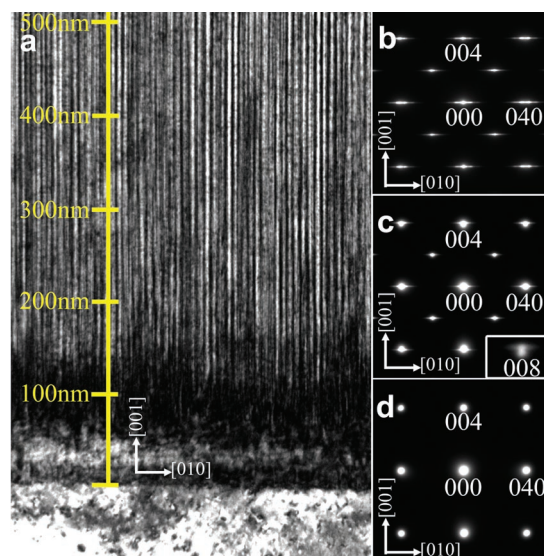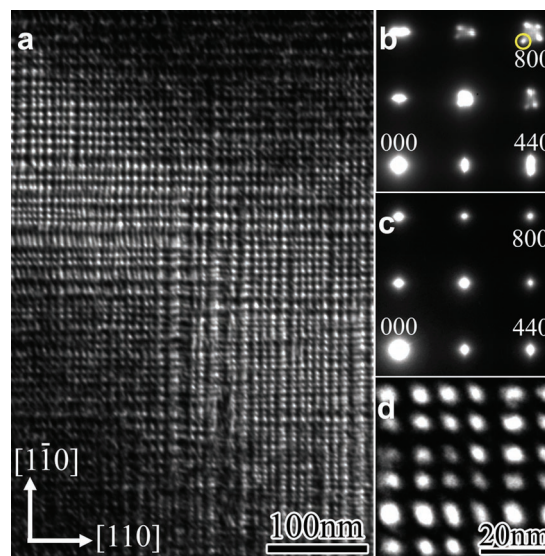

Figure 2. TEM side-view images for a ZnMnGaO$_4$ film. (a) A TEM bright field side-view image near the MgO substrate showing the nanostructured film, a thin transition layer, and the substrate, from top to bottom. The periodicity between the bright rods is ~6.2 nm. (b) A diffraction pattern near the film surface showing diffusive streaks perpendicular to the rod direction. (c) A diffraction pattern near the interface between the film and the substrate, showing both substrate and film peaks. Note that the diffusive streaks are weaker than those near the surface. (d) Electron diffraction of the MgO substrate only. No diffusive peaks are visible.

represent two chemically distinct nanorods: one is orthorhombic, and the other is cubic (tetragonal to be precise).

A bright-field TEM side-view image near the MgO substrate in Figure 2a unveils the details of the self-assembled nanorod structure. Long nanorods without defects are formed uniformly above a transition layer to the top surface of the film and reach ~750 nm in length. The transition layer in the film without any fringes (i.e., without nanorods) forms up to ~50 nm from the substrate. The periodicity between the bright rods is ~6.2 nm along the [010] direction, which implies that the length of the cross-sectional edge of a single square nanorod along [110] is ~4.4 nm. To clarify the details of the crystallographic structure, electron diffraction patterns of different regions of the side-view specimen have been

investigated. Figure 2b shows the diffraction image near the top surface of the film. Since the diameter of the probing size is ~450 nm, the bottom of the probing area is located at the ~400 nm level from the substrate in Figure 2a. Clear diffraction peak splitting of, for example, the (040) or (044) peak is evident, and this splitting originates from the presence of two types of nanorods with different crystallographic structures (this will be discussed in detail later). Note that the elongated diffusive streaks are also observed along the [010] direction (perpendicular to the nanorod growth direction), indicating the presence of either a small variation of the periodicity of the nanorods or nonuniform nanorod boundaries. No diffraction peak splitting was detected near the substrate (less than ~200 nm from the substrate) [Figure 2c]. The contributions of the nanorod region and the transition layer to the diffraction in Figure 2c are ~43% and ~14%, respectively. This depth dependence of the diffraction peak splitting is expected if the strain from the substrate is released with increasing distance away from the substrate. The lattice constants near the top surface have been calculated within this scenario. We have obtained the in-plane lattice constants of Mn-rich orthorhombic nanorods of $a_C^O \approx 8.01$ Å and $b_C^O \approx 8.92$ Å, while the in-plane lattice constant of the Mn-poor tetragonal nanorods is $a_C^T \approx 8.41$ Å, slightly larger than that of the phase-separated polycrystalline ZMGO ($a_C^B \approx 8.3$ Å).[11] Note, however, that the average in-plane lattice parameter (8.43 Å, taking into account the rotation of the Mn-poor regions, which will be further discussed below) of the nanorods even near the top surface is close to that of the MgO substrate (8.43/2 Å). The out-of-plane lattice constants for both nanorods are identical ($c_C^O \approx c_C^T \approx 8.23$ Å) and slightly smaller than that in the phase-separated polycrystalline ZMGO ($c_C^B \approx 8.3$ Å). These results are consistent with the presence of an average tensile strain in the film from the cubic MgO substrate all the way to the top of the film surface. We emphasize that we have deliberately chosen the MgO substrate to utilize the substrate-induced tensile strain to align nanorods, and this tensile strain, indeed, stabilizes the perfect orientation of nanorods. For the bulk polycrystalline ZMGO, the lattice parameters of neighboring Mn-rich and Mn-poor regions along the nanorods are identical (8.3 Å) and smaller than the average lattice parameter (8.4 Å) normal to the nanorod direction. Thus, the large lattice parameter (8.43/2 Å) of MgO induces a tensile strain on the film, resulting in [1] a slight expansion (from 8.4 Å to 8.43 Å) of the average lattice parameter normal to the nanorod direction, [2] a light contraction (from 8.3 Å to 8.23 Å) of the lattice parameter along the nanorods, and [3] the out-of-plane alignment of nanorods with the same lattice parameter (8.23 Å). Note that the identical magnitude of the out-of-plane lattice parameters of structurally and chemically distinct Mn-rich and Mn-poor nanorods is essential for the stable out-of-plane growth of nanorods over the extensive length of 750 nm. Furthermore, our results indicate that while the in-plane strain is released *locally* near the top surface, resulting in the diffraction peak splitting, the strain is *globally* maintained by keeping the average in-plane lattice constants close to the substrate lattice parameter


Figure 3. TEM top-view images for a ZnMnGaO$_4$ film. (a) A TEM dark field image near the top surface showing a checkerboard (CB) domain pattern. (b) A diffraction pattern near the top surface showing clear peak splitting, consistent with the presence of four types of domains. (c) A diffraction pattern near the substrate showing a tetragonally strained spinel structure without peak splitting. (d) Expanded view using one of the split peaks around the (800) position (yellow circle in Figure 3b). The size of each square nanorod varies from ~4 × 4 nm^2 to ~4 × 6 nm^2.

for the entire CB region regardless of the depth. Figure 2d shows the diffraction image of the substrate only. Note that the (022) diffraction peak in a spinel notation is forbidden in the MgO diffraction pattern (space group: $Fm\bar{3}m$, 4.216 Å).

Dark-field TEM planar-view images near the top surface (Figure 3a) obtained by using a diffraction peak confirm the existence of a CB pattern. The diffraction pattern in Figure 3b, where the electron beams were directed along the [001] axis, reveals the presence of two well-defined phases having orthorhombic and tetragonal structures, consistent with the side-view diffraction image near the top surface (Figure 2b). This pattern is also consistent with that for the CB regions in the polycrystalline ZMGO.[11] The expanded dark-field planar-view image (Figure 3d) using one of the split peaks around the (800) position (yellow circle in Figure 3b) clearly demonstrates the presence of a CB pattern and the structural (compositional) modulation of the film. The edges of each CB domain are along the [110] or [1−10] directions, and the size of each CB domain varies from ~4 × 4 nm^2 to ~4 × 6 nm^2. On the other hand, the diffraction image taken near the substrate (Figure 3c) indicates no peak splitting, which is consistent with Figure 2c. Both the planar-view and the side-view images near the substrate reveal a tetragonally strained spinel structure. In fact, the domain boundaries in TEM planar-view images near the substrate (above the transition layer; not shown) appear smeared because of the structural similarity of the two types of nanorods in that strained region.

Figure 4a shows synchrotron radiation X-ray diffraction results for the H−K, H−L, and K−L cross sections of the reciprocal space map (RSM) around the (044) peak of the
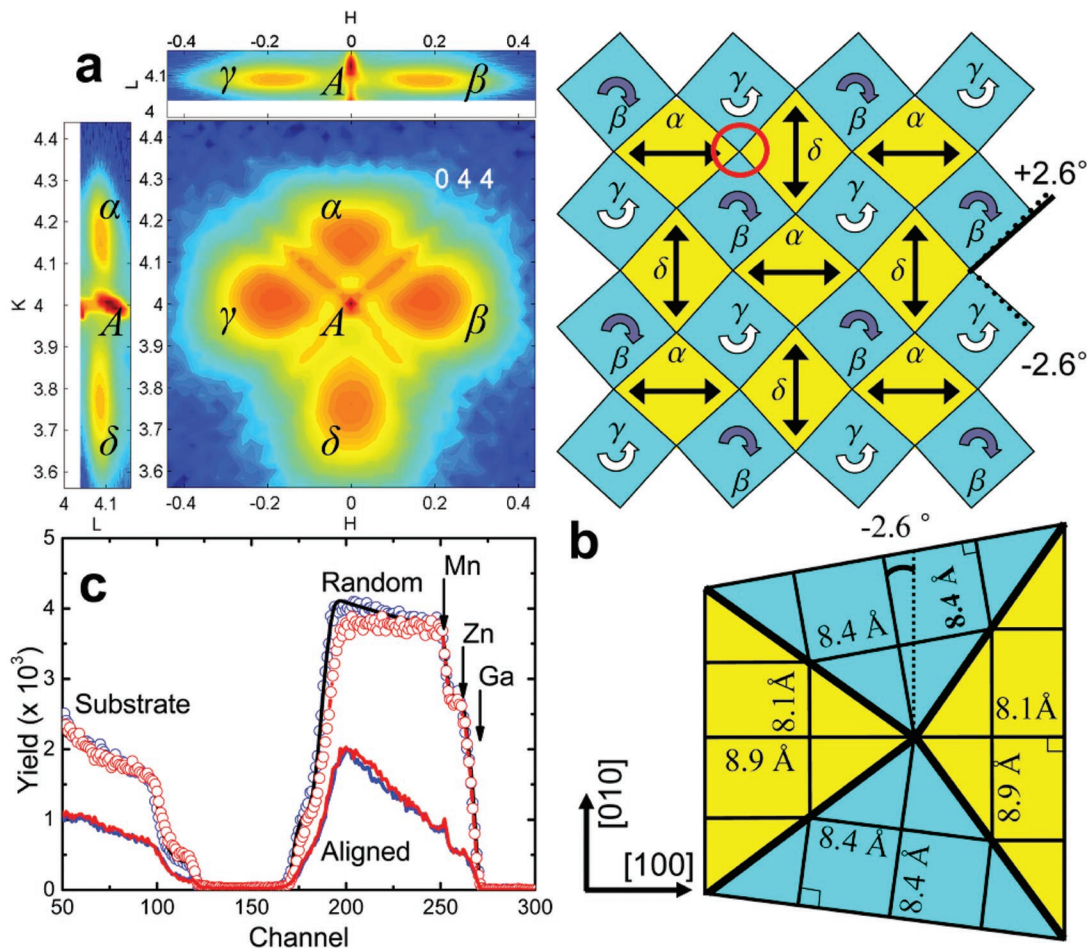
Figure 4. Reciprocal space maps and a schematic diagram representing the CB domain formation. (a) Synchrotron radiation X-ray diffraction intensity measured near the asymmetric (022) reflection of the MgO substrate ((044) of the spinel film). X-ray peaks corresponding to elastically strained tetragonal (A), rotated tetragonal (β and γ), and orthorhombic (α and δ) domains are shown in H$-$K, H$-$L, and K$-$L cross section reciprocal space maps (RSMs). (b) Schematic diagram showing the CB pattern formation. Yellow squares represent the orthorhombic domains, while blue squares are the rotated tetragonal domains. Solid straight arrows show the orthorhombic long axis direction, and curved arrows indicate the rotation directions of tetragonal domains. Bottom shows a cartoon for the coherent arrangement of tetragonal and orthorhombic unit cells at the corner of the domain boundaries (red circle in the top figure). (c) RBS spectra. Blue and red colors represent the as-grown and annealed films, respectively. The good match between the simulation shown with a black solid line and experimental data indicates that the chemical composition ($ZnMnGaO_4$) of as-grown films is that of the PLD target. Circles represent random orientation of the ion beam, while the solid lines correspond to aligned beams.

spinel structure. Three types of crystal structures (five different peaks) are evident in the H$-$K map. Four broad peaks, which are similar to (800) peaks in Figure 3b, are denoted as α, β, γ, and δ. The β and γ peaks are due to tetragonally distorted cubic domains, while the α and δ peaks are from orthorhombic domains.[11] The β and γ domains have the in-plane lattice constant of 8.41 Å and are rotated around L (film growth direction) by 2.6° in two opposite (clockwise and counterclockwise) directions, respectively. The α and δ domains are two perpendicularly oriented orthorhombic phases with the short (8.11 Å) and long (8.95 Å) in-plane lattice parameters. A schematic diagram representing the in-plane arrangement of these four types of domains forming the CB pattern is shown in Figure 4b. The bottom figure illustrates how the in-plane unit cells of the rotated tetragonal domains (β and γ in blue) and the neighboring orthorhombic domains (α and δ in yellow) share the edge (along the [110] direction) and form mutually coherent domain boundaries. The H$-$L and K$-$L cross sections of the RSM intensity in

Figure 4a confirm that the out-of-plane lattice parameters of each domain (α, β, γ, and δ) are identical (8.25 Å), which provides the means for the coexistence of these elongated domains in close contact throughout the volume of the film. Thus, the domain boundaries are coherent even along the c direction. This out-of-plane lattice parameter of 8.25 Å corresponds to -2.1% strain with respect to the MgO substrate. It appears that accommodation of -2.1% strain is provided by a combination of the orthorhombic distortions and the rotation of the tetragonal domains around the L direction. We emphasize that within experimental uncertainty, all estimated lattice constants from the results of the two-different-direction TEM diffraction and synchrotron X-ray scattering are consistent. Judging from the peak intensity analysis, the central peak, marked A in Figure 4a, corresponds to an ~120-nm-thick layer near the MgO substrate that shows the in-plane lattice parameter of 8.43 Å and thus is elastically strained with respect to the substrate. This layer exhibits the out-of-plane strain of -2.8% and

probably includes the ∼70 nm transition layer as well as the fully (i.e., locally as well as globally) strained initial nano-CB region. The presence of the diagonal narrow streaks with weak intensity suggests the presence of a residue of the high-temperature tetragonal phase, which we found to be dominant in unannealed films.

Averaged chemical compositions and the crystallinity of as-grown and oxygen annealed films were examined by Rutherford backscattering spectroscopy (RBS) (Figure 4c). Our simulations (black solid line) reveal that the as-grown film (open blue circles) has the same chemical composition as that of the (stoichiometric) PLD target. However, the random RBS yield from the annealed film (red open circles) shows a small difference in the slope of the spectrum (channels 180−250), indicating a slight ionic concentration gradient. These results indicate that annealing induces Mg diffusion into the film region. The Mg concentration near the substrate is at most 6% of the total atomic concentration. However, annealing seems to have a negligible effect on the film crystallinity, which is indicated by the identical yields of the RBS channeling spectra in the aligned geometry (red and blue solid lines). This observation suggests that the Mg incursion does not affect the crystal structure but is rather substitutional or segregated on grain boundaries in nano-CB regions near the substrate. Otherwise, the channeling of the annealed film should raise the RBS yield significantly higher, distinct from that of the as-grown film.[16] The channeling for both films reduces the RBS yield to ∼20% of the random level at the surface and to ∼50% at the interface, reflecting good crystalline quality. In the region of channels 50−120, a ∼50% reduction of the RBS yield is maintained (similar ratios at channel 200 and channel 100), indicating that the channeling fraction is continuous through the interface. This RBS result along with our TEM observation suggests that the formation of misfit dislocations at the film−substrate interface is not significant. Instead, the formation of the nanoscale twin structure realized by the ordered CB pattern may be the driving force to suppress the misfit dislocation formation in this film.[17] A similar reduction of the RBS yield on both annealed and as-deposited films demonstrates the highly coherent and stable structure of the films regardless of the coexistence of chemically different nanodomains, the long annealing time at 570 °C, and the ∼820 nm film thickness.

In conclusion, we have grown nano-CB ZMGO thick films on MgO substrates. The films are elastically textured with four types of domains with mutually coherent domain boundaries and the *average* in-plane lattice parameter close to that of the MgO substrate. The out-of-plane lattice parameters of two rotated tetragonal (Ga-rich) and two orthorhombic (JT active Mn-rich) domains are identical and significantly strained all the way to the top of the film surface. Regularly spaced nano-CB domains with an ∼8.8 nm edge periodicity relieve the volume strain energy and play an active role in reducing the formation of misfit dislocations, which is commonly observed in the conventional growth of highly mismatched films.[17−19] This new elastic film growth mechanism can produce a potential impact for the monolithic integration of lattice-mismatched materials with complementary electronic, magnetic, and optical properties.[20,21] Moreover, the self-assembled nano-structure with perpendicular nanorods exhibiting an unprecedented high degree of order provides an important alternative with practical functionalities to the conventional nanometer-scale fabrication of oxide materials.

Supporting Information Available: Material synthesis and experimental methods. This material is available free of charge via the Internet at http://pubs.acs.org.

References

(1) Lin., Y.; Böker, A.; He, J.; Sill, K.; Xiang, H.; Abetz, C.; Li, X.; Wang, J.; Emrick, T.; Long, S.; Wang, Q.; Balazs, A.; Russell, T. P. *Nature* **2005**, *434*, 55.

(2) Sun, S.; Murray, C. B.; Weller, D.; Folks, L.; Moser, A. *Science* **2000**, *287*, 1989.

(3) Shevchenko, E. V.; Talapin, D. V.; Kotov, N. A.; O'brien, S.; Murray, C. B. *Nature* **2006**, *439*, 55.

(4) Helveg, S.; Li, W. X.; Bartelt, N. C.; Horch, S.; Lægsgaard, E.; Hammer, B.; Besenbacher, F. *Phys. Rev. Lett.* **2007**, *98*, 115501.

(5) Jones, D. E.; Pelz, J. P.; Hong, Y.; Bauer, E.; Tsong, I. S. T. *Phys. Rev. Lett.* **1996**, *77*, 330.

(6) Brune, H.; Giovannini, M.; Bromann, K.; Kern, K. *Nature* **1998**, *394*, 451.

(7) Liu, X.; Lu, B.; Iimori, T.; Nakatsuji, K.; Komori, F. *Phys. Rev. Lett.* **2007**, *98*, 066103.

(8) Zheng, H.; Wang, J.; Lofland, S. E.; Ma, Z.; Mohaddes-Ardabili, L.; Zhao, T.; Salamanca-Riba, L.; Shinde, S. R.; Ogale, S. B.; Bai, F.; Viehland, D.; Jia, Y.; Schlom, D. G.; Wuttig, M.; Roytburd, A.; Ramesh, R. *Science* **2004**, *303*, 661.

(9) Zavaliche, F.; Zheng, H.; Mohaddes-Ardabill, L.; Yang, S. Y.; Zhan, Q.; Shafer, P.; Reilly, E.; Chopdekar, R.; Jia, Y.; Wright, P.; Schlom, D. G.; Suzuki, Y.; Ramesh, R. *Nano Lett.* **2005**, *5*, 1793.

(10) Ramesh, R.; Spaldin, N. A. *Nat. Mater.* **2007**, *6*, 21.

(11) Yeo, S.; Horibe, Y.; Mori, S.; Tseng, C. M.; Chen, C. H.; Khachaturyan, A. G.; Zhang, C. L.; Cheong, S.-W. *Appl. Phys. Lett.* **2006**, *89*, 233120.

(12) Zhang, C. L.; Yeo, S.; Horibe, Y.; Choi, Y. J.; Guha, S.; Croft, M.; Cheong, S.-W.; Mori, S. *Appl. Phys. Lett.* **2007**, *90*, 133123.

(13) Guiton, Beth S.; Davies, Peter K. *Nat. Mater.* **2007**, *6*, 586.

(14) Ivanov, M. A.; Tkachev, N. K.; Fishman, A. Ya. *Low Temp. Phys.* **1999**, *25*, 459.

(15) Zhang, C. L.; Tseng, C. M.; Chen, C. H.; Yeo, S.; Choi, Y. J.; Cheong, S.-W. *Appl. Phys. Lett.* **2007**, *93*, 233110.

(16) Wielunski, L. S.; Hashimoto, S.; Gibson, W. M. *Nucl. Instrum. Methods Phys. Res. B* **1986**, *13*, 61.

(17) Schmidt, Th.; Kroger, R.; Flege, J. I.; Clausen, T.; Falta, J. *Phys. Rev. Lett.* **2006**, *96*, 066101.

(18) Jain, S. C.; Harker, A. H.; Cowley, R. A. *Phil. Magazine A* **1997**, *75*, 1461.

(19) Sun, H. P.; Tian, W.; Pan, X. Q.; Haeni, J. H.; Schlom, D. G. *Appl. Phys. Lett.* **2004**, *84*, 3298.

(20) Thompson, D. A.; Best, J. S. *IBM J. Res. Dev.* **2000**, *44*, 311.

(21) Duan, X.; Lieber, C. M. *Adv. Mater.* **2000**, *12*, 298.

NL072848S